Seismic response to deep injection changes at Rotokawa geothermal field, New Zealand

Chet Hopp[1]

[1]Victoria University of Wellington

February 18, 2019

Abstract

While simple spatial locations of seismicity can provide valuable insights about reservoir structure and fluid movement, frequency-magnitude distributions, often of secondary interest to operators, may contain unique information about the distribution of pressure. In this work, we present a four-year catalog of seismicity for the Rotokawa geothermal field in the central Taupō Volcanic Zone, New Zealand starting two years after the commissioning of the 140 MW Nga Awa Purua power station. Using waveform-correlation based signal detection we double the size of the previous earthquake catalog and update the location and orientation of two important reservoir faults, while potentially identifying a new structure. We find the rate of seismicity to be insensitive to major changes in injection strategy during the study period, including the injectivity decline and shift of injection away from the dominant injector, RK24. We also map the spatial distribution of the earthquake frequency-magnitude distribution, or b-value. Although complex, the spatial variation of b can potentially be used to monitor the relative distribution of pressure in the reservoir, where areas of high b correspond to areas of high pore-fluid pressure and a broad distribution of fractures. While not routinely conducted, we believe our results show promise for using earthquake b-value as an additional tool for reservoir monitoring and management.

1 Introduction

Geothermal operators routinely monitor rates and locations of microseismic activity at developed reservoirs. Typically, the location of seismicity is assumed to correlate with regions where pore-fluid pressure has been artificially elevated by fluid injection (e.g. Sherburn et al., 2015; Garcia et al., 2016). In turn, these areas are assumed to correspond to major flow pathways in the reservoir, which are of paramount importance in understanding reservoir dynamics and planning injection/extraction well targets. In addition, reservoir structures can be accurately imaged from high-precision earthquake hypocentral locations as can the extent of the permeable reservoir (Sewell et al., 2015a).

However, much of the information contained in even a basic earthquake catalog can go unused by reservoir managers. Specifically, while earthquake magnitudes are nearly always calculated during automated processing of seismic data, this information goes relatively unnoticed. In a limited number of cases (e.g. Bachmann et al., 2012), magnitude information has been used to infer reservoir properties such as pore-fluid pressure and the extent of fracturing. Given the inclusion of event magnitude data in nearly every earthquake catalog, more attention should be paid to patterns in frequency-magnitude distributions as a tool for reservoir management.

In this paper we focus on the Rotokawa geothermal field in the central Taupō Volcanic Zone of New Zealand. The field was initially developed in 1997 but has undergone large-scale development since that time, most significantly the commissioning of the 140 MWe ("megawatts electrical") Nga Awa Purua plant (NAP) in 2010 (McNamara et al., 2016). The seismic dataset analyzed here (2012–2015) corresponds to a period of stabilization, during which the reservoir was equilibrating to the increased extraction required by the

Field	Operation	Start	End
Rotokawa	RK24 Injectivity Decline	2012	2013
Rotokawa	Switch of Injection: RK24-RK23	June-2014	July-2014
Rotokawa	RK34 Drilling Losses	September-2014	November-2014
Rotokawa	Plant Shutdowns and Startups	2012-2015	2012-2015

Table 1: Period of interest defined by Mercury for 2012–2015

installation of NAP. We use a matched-filter earthquake detection technique to substantially increase the number of events in our catalog relative to standard, automatic detection. We then calculate magnitudes for the newly detected events, again using a waveform correlation-based technique before precisely relocating each event.

In the following analyses, we compare our catalog to the catalogs of previous studies of microseismicity at Rotokawa (Sewell et al., 2015a; Sherburn et al., 2015) and relate the rate and location of seismicity to changes in injection strategy at Rotokawa. We also map the frequency-magnitude distribution (b-value) within the field, something which has not been done at Rotokawa before. While the observed patterns in b-value are quite complex, when combined with high-precision locations, they show potential for mapping of pore-pressure and/or fracturing extent at a reservoir scale.

1.1 Rotokawa resource development

As with most of the Taupo Volcanic Zone geothermal fields, the existence of the Rotokawa resource was originally verified through a New Zealand government-funded drilling program starting in the 1960's (Cole and Legmann, 1998). The first resource consent was granted to the Tauhara no. 2 Trust and various other entities in 1993 with electricity generation beginning in 1997 with the installation of the 24 MWe 'RGEN' combined-cycle power plant (Legmann and Sullivan, 2003). In 2000, Mercury NZ, Ltd. (then Mighty River Power) combined with the Tauhara no. 2 Trust to form the Rotokawa Joint Venture, which continues to oversee development at Rotokawa at present (Legmann and Sullivan, 2003).

Prior to 2005, reinjection at Rotokawa was done at depths of <1000 m (Sewell et al., 2015b) but was moved to greater depths (1000-3000 m) due to pressure buildup in the shallow injection zone (McNamara et al., 2016). Additional resource consents were granted to the Rotokawa Joint Venture in 2007, prompting the drilling of more than ten additional wells (RK19-RK35) and culminating in the commissioning of the Nga Awa Purua (NAP) plant in 2010, bringing the total installed capacity at Rotokawa to 174 MWe fed by 60,000–65,000 t/d of fluid from the reservoir (McNamara et al., 2016). The additional information provided by the new wells allowed for significant improvements to the reservoir conceptual model detailed by Sewell et al. (2015b) and McNamara et al. (2016).

1.2 Rotokawa operations changes

The dataset analyzed in this work spans the four years starting in 2012 and ending at the start of 2016. During this period, little new development was undertaken at Rotokawa, as the resource was adjusting to the significant increase in production associated with the startup of NAP in 2010. Changes in injection and production are therefore more subtle than those analyzed at the nearby Ngatamariki for the same period, where the drastic changes were associated with well stimulation and power plant commissioning (Clearwater et al., 2015). However, Mercury have identified a number of periods between 2012 and 2015 during which the character of seismicity may help address various outstanding questions about the nature of the reservoir:

As is typically the case for produced reservoirs of any type (e.g. natural gas, oil, geothermal), seismicity at Rotokawa is caused predominantly by the injection, not the extraction, of fluids. This is because injection

increases pore fluid pressure, thereby destabilizing fracture networks, whereas extraction achieves the opposite, although stress changes induced by the removal of reservoir volume are non-negligible in triggering earthquakes (Segall, 1989; of Sciences, 2013). For this reason, the periods defined by Mercury correspond predominantly to changes in injection operations. The first two, in Table 1.2, correspond to a period of injectivity decline in the dominant injection well RK24 (Figure 1) due to an unknown cause. In response to the well's declining ability to accept injectate from the power plants, excess fluid was shifted to well RK23 (Figure 1).

From September to November 2014, Mercury drilled an additional production well, RK34. At reservoir depths, the drilling operation incurred full fluid losses. Similar drilling losses induced a large number of seismic events during drilling in southern Ngatamariki (Hopp et al., 2019) and may have had a similar effect at Rotokawa. Finally, as noted by Sewell et al. (2015a), swarm-like behavior (which they defined as a day on which more than 15 events occurred) has been observed at Rotokawa in the past and is thought to be related to pressure perturbations induced by power plant shutdown and startup during regular maintenance operations.

The fluid injected at Rotokawa varies by application and between individual wells. For instance, during the drilling of RK34, the drilling fluid was composed predominantly of water at an ambient temperature of 10–20°C. During standard plant operations, the injectate at each injection well can be condensate (the product of cooling the steam used to turn the turbines), concentrated brine (brine with condensate removed) or some combination of these end members. During most of the period studied here, brine and condensate from NAP were injected into RK23-24, while the injectate from RGEN was injected into RK20. Injected fluid, regardless of the source, entered the injection wells at a temperature between 80 and 130°C.

1.3 Reservoir model

The behavior of the Rotokawa reservoir is dominated by three known NE-SW striking faults, each named for its location relative to the injection or production field. From east to west they are: the Injection Field Fault (IFF), Central Field Fault (CFF) and Prodution Field Fault (PFF) (Wallis et al., 2013) (Figure 1). The existence and orientation of these faults is known from well cuttings that show vertical offsets in the top of the Rotokawa Andesite (and other units) between wells. The CFF, for instance, is credited with a vertical displacement of nearly 400–500 m between the injection and production wells, while the IFF and PFF represent vertical displacements of 250–350 m (Wallis et al., 2013). A number of independent datasets have been used to corroborate the presence of these faults, including tracer returns (Addison et al., 2015, 2017), pressure compartmentalization (Quinao et al., 2013; Sewell et al., 2015b) and previous studies of microseismicity (Sherburn et al., 2015; Sewell et al., 2015a).

Large lateral pressure gradients within the Rotokawa reservoir indicate that it is made up of several discrete compartments that either have different permeability or are separated by structures acting as cross-strike flow barriers (Quinao et al., 2013; Sewell et al., 2015b). The major faults mentioned above act either as barriers between these compartments or as conduits for fluid flow within compartments. Slow or nonexistant tracer returns from injection to production indicate that the CFF is such a barrier, isolating the injection compartment from each of the production compartments (Figure 1). However, this isolation is not constant along the strike of the CFF (Addison et al., 2017). Current modeling by Mercury suggests that a 'leaky' connection exists between the main injection well, RK24 and the central production wells (RK5, RK14, RK29, blue polygon in Figure 1), which provides pressure support to these production wells. This pressure support is not present in the west (4.2 MPa drawdown) or northern (3 MPa drawdown) production field compartments (Quinao et al., 2013; Addison et al., 2017) (green and red, respectively in Figure 1).

Strong pressure connection between the wells within the western production compartment suggests that the PFF acts as an along-strike fluid conduit, transmitting pressure signals quickly to distances of up to a kilometer (Quinao et al., 2013; Sewell et al., 2015b; McNamara et al., 2016). These pressure observations are well correlated with the geologic offsets observed in the well cutting mentioned above (Wallis et al., 2013).

There is less evidence to suggest what role the IFF may play in reservoir behavior, as the only well completed to the east of the structure is RK23. Although tracer was injected into RK23 in 2011, issues with isotope breakdown rendered much of the test inconclusive. Bottom hole temperatures are some 40°C hotter in RK20 and 24 than in RK23, at only ~200 m distance and some evidence suggests that there is significant pressure connection between all injection wells (Quinao et al., 2013). However, RK23 has traditionally accepted a smaller proportion of overall injection, so trends associated with changes there may be difficult to separate from the rest of the injection wells.

1.4 Previous work

The only previous studies of the seismicity at Rotokawa were conducted for the years 2008–2012 by workers at GNS Science and Mercury (formerly Mighty River Power) (Sherburn et al., 2015; Sewell et al., 2015a). These studies detailed a pattern of seismicity that shifted with time as the injection and production strategies evolved in response to field development and reservoir understanding. At of the end of 2012 (the start of the dataset presented here), Sherburn et al. (2015) identified the currently-active area of seismicity as that bounded by the white, dot-dashed diamond shown in Figure 1. This cluster of seismicity occurred at the approximate depth of the permeable zones in wells RK20, RK23 and RK24, which accounted for nearly all of the deep injection into the Rotokawa reservoir at the time. This cluster was inferred to be bounded to the northwest by the CFF (Figure 1), corroborating the evidence from tracer testing that fluid flow was impeded across the structure, thus allowing pressure buildup east of the fault and inducing seismicity (Sherburn et al., 2015; Sewell et al., 2015a).

Sherburn et al. (2015) and Sewell et al. (2015a) cited the relatively modest wellhead pressures measured in the injection field (<1.5 MPa) as evidence for cooling-dominated, and not pressure-dominated, triggering of seismicity at Rotokawa. However, we feel that evidence is limited to support this claim, given that stress changes as low as 10^{-2} MPa have been shown to trigger seismicity in many settings (Stein, 1999; Keranen and Weingarten, 2018). As Sewell et al. (2015a) noted, the large temperature gradients induced at the injection wells (>180°C) certainly produce stress changes of tens of MPa within 10-100s of meters of the well, especially when large volumes are injected over years (Stephens and Voight, 1982). Though the effect of cooling on fracture stability is complex (Jeanne et al., 2015b), these cooling effects likely do dominate earthquake triggering close to the injection wells. However, the occurrence of seismicity beyond a ~500 m radius and the lack of measured cooling at the production wells (including those that receive pressure support from the injection zone) indicate that other effects, including pore pressure increase and poroelastic stress transfer play a role in earthquake triggering (Schoenball et al., 2012).

2 Data and methods

2.1 Data

As described in detail in (Hopp et al., 2019, submitted), the Mercury seismic network covers an area of approximately 450 km^2 surrounding the Rotokawa and Ngatamariki geothermal areas. While most of the instruments are Mercury-owned 4.5 Hz Geospace GS-11D short-period geophones, we have also incorporated a number of stations operated by Contact Energy at their nearby Wairakei geothermal field, as well as three broadband instruments and one short-period instrument operated by the GeoNet national network (Table **Reference station table**). At any one time from 2012–2015, as few as 15 and as many 29 instruments were operational.

GNS Science, under contract with Mercury, provided the initial earthquake catalog used in this study. The raw waveform data were collected quarterly from Mercury's data loggers and supplemented by data from the aforementioned GeoNet stations. Events were automatically detected and located using the SeisComP3 software package (**?**). We threw out all events located >5 km outside the bounds of the Rotokawa resistivity

boundary (yellow shaded area, Figure 1), so that a total of 3225 microearthquakes of between M_L 0.37 and 3.68 remained. We relocated these events using both the nonlinear location program *NonLinloc* (Lomax et al., 2014) and the double-difference relocation software *GrowClust* Trugman and Shearer (2017) prior to undertaking the following analyses.

Production and injection well locations, temperatures, flow rates and pressures were provided by Mercury.

2.2 Matched-filter detection

We used the matched-filter correlation detection approach described by (**?**Hopp et al., 2019) to increase the number of events included in the GNS Science earthquake catalog mentioned above. This approach significantly increases the number of events detected without unduly increasing the rate of false detection and is well suited to detection at geothermal fields that are subject to noise sources and dense clusters of small seismic events.

Each of the 3225 events taken from the preliminary GNS Science catalog was used as a 'template' event. Each template consists of one-second-long waveforms, starting 0.1 seconds before the P-pick. We chose not to use the horizontal channels after inspection of the GNS automatic S-picks revealed a significant number of mis-picked arrivals. After applying an anti-aliasing filter, both raw and template waveforms were sampled at 50 Hz and filtered from 3.0 to 20.0 Hz.

To generate detections, templates were cross-correlated with continuous data at a rate of 50 samples per second. At each sample, the cross-correlation coefficients for each channel of data were summed to create the network detection statistic (**?**). A detection was recorded whenever the detection statistic exceeded a threshold value, which in this case was defined as the daily median absolute deviation (MAD) of the detection statistic multiplied by eight (as suggested by **?**).

Duplicate removal was conducted by looping through all detections in order of descending detection statistic and removing detections within a user-defined time buffer of two seconds. We adopted two seconds for the time buffer following a visual review of template events that revealed numerous cases of near-repeating seismicity with inter-event times of 3–5 s.

Visual inspection of a subset of the detection waveforms showed that false detections occurred at a rate of approximately 1–3 false detections per day. However, there are too many detections to inspect them all manually. Therefore, we employ a sequence of thresholds based on the correlation between the template and detected waveforms in order to exclude lower-quality events, thus suppressing the number of false detections in our final catalog. These thresholds were applied during the location and magnitude calculation procedures described below. We visually inspected thousands of waveforms from the final catalog while manually picking first motion polarities and did not encounter a single false detection.

2.3 *NLLoc* locations

For each newly-detected event, P-picks were made at each channel included in the template via an automated workflow. For each station, the template and detected waveforms were correlated over a 0.2 second window centered at the detection time. Picks were recorded at the time corresponding to the highest correlation value within that window. If the correlation value of the template and detected waveform fell below 0.4, the pick was discarded. We then discarded those events with five or fewer picks. For the remaining events, we made automatic S-picks using the method developed by **?** and modified by **?**, a process detailed by (**?**). We located the remaining events with the nonlinear location program *NonLinLoc* (Lomax et al., 2014) using a preliminary 1-D model computed using the program *VELEST* (**?**Sewell et al., 2017)**Methodology V-mod Table**.

2.4 Magnitudes

Magnitudes were calculated for each of the newly-detected events using an approach originally developed by **?**. The specific approach used here is described in detail in Hopp et al. (2019), but relies on the assumption that the relative amplitude between a template event (for which a magnitude was calculated by GNS Science) and the detected event represents their relative moment. This relative moment can then be used to calculate the magnitude of the detected event.

We calculated relative amplitudes only when the cross-correlation coefficient between the template and detection exceeded 0.6 at any given station. For event pairs with a minimum of four common stations exceeding the correlation threshold, we calculated the relative moment as the median of the relative amplitudes, following **?**. As the relative amplitudes are calculated from waveforms recorded at the same station, there is no need to remove the instrument response.

We used the template M_L to calibrate the relative moment calculations from the method above and produce M_L estimates for each detection. This was done by first converting the template M_L to M_w using the scaling relationship

$$M_L = 0.88M_w + 0.73 \tag{1}$$

determined for locally detected, shallow New Zealand earthquakes (**?**) and then converting to seismic moment using the well-known equation

$$M_w = \frac{2}{3}\log_{10} M_0 - 9$$

(**?**). Knowing the relative moment of the template event from the procedure outlined above, we then determined the relationship between the relative moments and actual moment which allowed us to convert relative moments to M_w and then back to M_L using Equation 1. After applying this methodology, 28,414 events remained in our catalog.

2.5 *GrowClust* locations

Finally, the entire catalog was relocated using the double-difference relocation program *GrowClust* (Trugman and Shearer, 2017) with differential travel times generated using the Python package *hypoDDpy* (**?**) using a 1 s correlation window, a maximum time shift of 0.2 s and a minimum cross-correlation value of 0.6. The final double-difference relocations are shown in Figure 2.

2.6 b-value Calculation

The frequency-magnitude relationship for earthquake catalogs is a power-law distribution described by

$$\log N = a - bM$$

(Gutenberg and Richter, 1942) where a increases with the number of earthquakes in the catalog and b describes the distribution of earthquake magnitudes above the catalog magnitude of completeness (M_c). We calculate M_c for the catalogs presented here following the methodology of Wiemer and Wyss (2000). For a range of M_c values, a and b are determined for our earthquake catalog and an idealized synthetic distribution constructed with the same a and b values. The difference between the synthetic and measured distributions is then minimized to find the most appropriate M_c.

We then map catalog b-value in space using the approach of Bachmann et al. (2012), wherein, for each event in the catalog (which they refer to as a 'focus'), the nearest n events are selected and M_c is calculated for this subset. If the number of events above M_c exceeds a threshold, the b-value is calculated and mapped to the focus event using the maximum-likelihood method (Aki, 1965; Shi and Bolt, 1982). Bachmann et al. (2012) map the b-value for the 150 nearest events, with a threshold of 25 events greater than M_c. Here we use the nearest 300 events with a minimum threshold of 100 events above M_c.

3 Results and Discussion

3.1 Locations and magnitudes

The *GrowClust* relocations of the final 6479 events are shown in Figure 2. From a field-wide perspective, the location of seismicity has changed little from that presented by Sherburn et al. (2015) and (Sewell et al., 2015a). The area of seismicity identified in their studies is overlain on Figure 2 (black dot-dashed diamond) for context and broadly agrees with the extent of the densest seismcity in our catalog. Most events occur in the northeastern portion of the field, between the northern injection wells (RK20, 23, 24) and the northern production wells (RK13, 14, 25, 29, 30), with some events extending further towards the north and east. The northwest portion of the field, north of the Waikato River, as well as the southern injection zone (near wells RK21-22) correspond to areas of little seismicity. Within the area of densest seismicity, however, our catalog more clearly reveals subclusters and structure than previous studies, which identified only one uniform area of dense seismicity (Sherburn et al., 2015). We discuss the implications for these structures in the following sections, while the potential causes of the location variations between this and previous work are detailed in Appendix 7.1.

In Figure 3A, we show the frequency-magnitude distribution for the GNS template events (dotted) and final detected events (solid) for which we calculated a b-value of ~1.09±0.02, comparable to b-values in areas of hydrothermal activity worldwide, and similar to those calculated at the Ngatamariki geothermal field, located ~7 km to the north (Figure 3B) (e.g. Bachmann et al., 2012; Wiemer and McNutt, 1997; Dinske and Shapiro, 2012; Hopp et al., 2019). In areas of active volcanism as well as in both hydrocarbon extraction and geothermal settings, b-values far exceeding 1.0 are reported (Dinske and Shapiro, 2012; Shapiro et al., 2011). In general, b-values above 1.0 have been attributed to the presence of fluids and high pore-fluid pressures. It may be that such elevated pore pressure allows fractures to fail that are non-optimally oriented in the local stress field. As the differential stress acting on these non-critically stressed structures is smaller than on those which are critically stressed, more small-magnitude events will occur than for naturally-occuring events (Bachmann et al., 2012). It has been suggested that the presence of a strong thermal gradient (e.g. related to an intrusion or injection of cold water) could aid in development of small, tensional fractures with orientations normal to the prevailing structural fabric (Warren and Latham, 1970). In conjunction with elevated pore pressure, such an effect would raise the *b*-value above naturally-occurring values.

Figure 3B shows the *b*-value at Rotokawa in comparison to the values for the two clusters of seismicity at the Ngatamariki geothermal field calculated by Hopp et al. (2019). The *b*-value at Rotokawa is most similar to that of the southern injection zone at Ngatamariki, likely because both areas encompass major structures >1 km in length that are able to accommodate larger-magnitude earthquakes. As described by Hopp et al. (2019), the high *b*-value in northern Ngatamariki is likely related to intense intrusive-related alteration, which has produced a fracture population that is relatively devoid of large structures, limiting the likelihood of producing larger events.

3.2 Compartmentalization

As shown in Figure 1 and discussed in Section 1.3, the Rotokawa reservoir is known to be broken into a number of compartments, with at least three in the production field and one in the injection field. Patterns in seismicity are of little use in delineating the borders of the production field compartments because relatively few earthquakes occur in that portion of the field. However, we believe that our relocations (Figs. 2 and 4) allow for further constraint on the location of the Central Field Fault and Injection Field Fault, and may provide evidence for previously unidentified subcompartments within the injection field.

There are at least two NE-SW-striking sub-linear features revealed by this catalog, outlined and labeled in bold red in Figure 4B. One feature lies between the injection and production fields, taking on an arcuate shape, concave towards the southeast. This structure likely defines the CFF as it sits between the injection field and the central production compartment, as previously modeled by Wallis et al. (2013). The other

structure strikes NE-SW between wells RK20/24 and well RK23, and extends towards the northeast. We therefore interpret this to be the IFF, again due to the consistency of its location with known geologic and temperature offsets. The IFF, specifically, was not previously imaged by microseismicity, nor was there an obvious offset between what appear to be CFF-related and IFF-related events (Sherburn et al., 2015). We suggest three possible reasons for this.

One, we are able to more clearly define structures as a result of the larger number of events in our catalog. Two, the change in algorithm used for the double-difference relocation (*GrowClust*, in our case) was more stable in the presence of noisy data than *HypoDD* (see Appendix 7.1). Three, the location changes actually reflect reservoir-scale changes in permeability and fluid flow from 2012 to 2015. We support the view that the location discrepancy is rooted in the processing workflows used. We assert that the tighter clustering exhibited in our catalog and the clear relation of hypocenters to the known faults in the reservoir lend confidence to our interpretation.

A third potential structure is outlined in dotted red striking NW-SE (Figure 4). On visual inspection, this feature is less obvious than those of the CFF and IFF and we therefore assign less confidence to its existence. Furthermore, no major cross-strike (NW-SE) structures have been identified from offsets in well cuttings. However, along-strike variations in pressure drawdown and tracer returns do indicate that the reservoir is likely divided not only by NE-SW-striking structures, but NW-SE-striking structures as well (Sewell et al., 2015b; Quinao et al., 2013). Specifically, the contrast between the >4 MPa drawdown in the western production field (green box, Figure 1) and the 3 MPa drawdown at the northern production wells (red box, Figure 1) lends weight to the existence of NW-SE structures.

The following analysis is based on the hypothesis that pressure differentials between compartments may exhibit as variations in seismic characteristics. Therefore, we have divided the area of densest seismicity into three potential compartments bounded loosely by the inferred locations of the major faults and the potential NE-SW structure mentioned above (Figure 4). The light green polygon in Figure 4B will be referred to as the western compartment and the coral and pink polygons will be referred to as the northeastern and southeastern compartments, respectively. These divisions are based on hypocentral locations only and constitute potential compartments that have not been identified previously.

3.3 Compartment characteristics

For a first-order view of the properties of seismicity in the compartments defined in Figure 4, we plot the cumulative number of events in each (total number and normalized number: Figure 5A-B) as well as their respective frequency-magnitude distributions (Figure 5C). Panels A and B do not reveal striking differences in the rate of seismicity between compartments, with the exception of an increased rate of events in the northeast compartment (coral-colored) relative to the others at the end of 2012, which will be investigated in Section 4. However, panel C reveals a significant variation in b-value between compartments. While the western and northeastern compartments have b-values of 0.93 ± 0.05 and 1.03 ± 0.03, respectively, the b-value in the southeast compartment is markedly higher (1.16 ± 0.03). Given that the southeast compartment is the closest to the main injection wells (RK20, 23 and 24), this may suggest that the b-value at Rotokawa is proportional to pore-fluid pressure, which is most elevated near injection wells. A similar effect was observed by Bachmann et al. (2012) at the Basel injection site in Switzerland, who found b-values >2.0 near the injection interval.

To further investigate this observation, we mapped the b-value variation in space and time using the methodology detailed in Section 2.6, the results of which are detailed in Section 5, below.

4 Temporal variations in seismicity and injection parameters

Characteristics of seismicity are used by geothermal operators to supplement more traditional, well-based pressure and temperature measurements for reservoir management. At Rotokawa, microseismicity has been used to constrain the location of major structures such as the CFF as well as the base of the reservoir (inferred from the cutoff in seismicity with depth). As outlined in Section 1.2, the Rotokawa reservoir behaved unexpectedly during specific periods in our dataset. We address these periods below and comment on the implications for processes occurring in the reservoir.

4.1 RK24 injectivity decline

Starting at the beginning of 2012, RK24, the largest injection well by percentage of injection at Rotokawa, began to suffer a decline in injectivity, meaning that it could no longer accept the same volume of fluid for a given wellhead pressure (Figure 6A). This is a significant issue, because economical power plant operation requires a set enthalpy from a reservoir, which demands a set quantity of fluid to be extracted and injected. If a well cannot accept the fluid budgeted for it, that fluid must be shifted elsewhere, which can have negative implications for resource management. In the case of RK24, the fluid was shifted to both shallow injection well RK12 and deep injection well RK23, which injects into the reservoir on the opposite side of the IFF from RK24.

As the feedzones at RK24 (and RK20) are located to the west of the IFF and may therefore be better hydraulically connected to the western compartment (Figure 4), we expect seismicity in the western compartment to respond most readily to injection changes at these wells. Western compartment seismicity and relevant RK24 injection parameters are summarized in Figure 6. Injectivity begins to decline in the first half of 2012, after which Mercury made the decision to switch injection away from RK24. The switch can easily be seen as drops in flow rate, WHP and injectivity in July 2013 and again in July 2015.

The response in western compartment seismicity to the injectivity decline and subsequent decrease in flow at RK24 is subtle. The decrease in injectivity corresponds to a small increase in WHP between the start of 2012 and July 2013. This is possibly accompanied by a slight increase in the weekly number of events, which would be expected for a pressure increase (Figure 6B), but we do not assign much confidence to this observation. In addition, the drop in WHP in July 2013 from ~1.3 to 0.2 MPa does not produce the expected drop in the rate of seismicity. While the injectivity decline, and in particular the subsequent pressure drop might be expected to produce significant changes in the character of seismicity, there are a number of reasons why this may not be the case. The most significant complication to interpretation is that RK24 is not the only injector in this part of the field. Even if the pressure signals from RK23 and RK24 are isolated by the IFF, RK20 (on the same side of the fault as RK24) remained a significant injector throughout the dataset, injecting at a roughly constant rate of 600 t/h and a wellhead pressure of approximately 0.4 MPa. This may have provided enough pressure support in this section of the reservoir to continue to induce seismicity at close to previous rates. In addition, even as pressure had dropped at RK24, the injection rate was still ~800 t/h. As Sherburn et al. (2015) and Sewell et al. (2015a) have postulated, Rotokawa seismicity is likely affected more by stress changes induced by reservoir cooling than reservoir pressure increases, especially near the well. The results in Figure 6 may support this view as seismicity seems insensitive to pressure perturbations of up to 1 MPa at the wellhead, which are normally more than sufficient to induce seismicity (Keranen and Weingarten, 2018; Stein, 1999).

4.2 RK23 halt and restart

Most of the excess injection produced by the RK24 injectivity decline was accounted for by shallow injection into well RK12 (in the current production field) and deep injection into RK23. RK23 was being used as an injector for RGEN condensate until late 2012, when it was shut for 8 months (gray bar, Figure 7) before resuming injeciton (Addison et al., 2017). In Figure 7, we plot characteristics of seismicity in the

compartments that we interpret to be east of the IFF, where the pressure signal from RK23 is assumed to be the strongest. Similar to the western compartment, the rate of seismicity is mostly constant over time. Interestingly, the northeast compartment, furthest from RK23, experienced an increase in the rate of seismicity during the 8 months when no injection was occurring at the well, whereas the southeast compartment did not. This increased rate of seismicity is still significantly lower than in the compartment near the well, but it is unclear why seismicity further from the well would respond more strongly to a pressure perturbation than seismicity nearer to the well.

4.3 Aseismic injection: RK34 Drilling and RK21-22

One new well, RK34, was drilled at Rotokawa during our dataset. Although RK34 drilling incurred full fluid losses at reservoir depths, there was no discernible response in seismicity near the well, or anywhere else in the reservoir. This behavior is distinct from the similar case of NM10 drilling in Ngatamariki the year before, which induced a significant number of events (Hopp et al., 2019). However, aseismic injection is not uncommon at Rotokawa or Ngatamariki in general (Sewell et al., 2015a). For instance, drilling, and stimulation at well NM09 in Ngatamariki was largely aseismic, and injection into the southwestern injection wells, RK21/RK22 at Rotokawa has historically been aseismic (Hopp et al., 2019; Sewell et al., 2015a).

The case of RK21-22 is particularly puzzling, because RK21 was used as the dominant injection well from NAP startup (>1000 t/h) until 2011, but seismicity has never been observed in this section of the field (Sewell et al., 2015a). What's more, temperature and permeability in RK21-22 are highly similar to RK20-24. Why, then, does seismicity occur at one and not the other? Modeling at the Geysers geothermal fields has shown that density driven, downward flow can drive stabilization of the reservoir fracture network in regions where σ_1 is vertical (such as at Rotokawa) (Jeanne et al., 2015a). Although such an effect may help explain a lack of near-well seismicity in general, it does not explain the discrepancy between wells with such similar characteristics.

4.4 'Swarm' activity

Sewell et al. (2015a) and Sherburn et al. (2015) have observed periods of 'swarm-like' activity (defined as days with >15 events) at Rotokawa that may coincide with pressure perturbations caused by plant maintenance shutdown and startup periods. To determine if such behavior is also present in our catalog, we have plotted red bars in Figures 6, 7 and 8 indicating the times of plant shutdowns. The two shutdowns in 2012 (Figure 8) appear to be associated with 'swarm' events, defined here as days with more than 30 events due to the larger number of events in our catalog. However, the rest of the shutdowns appear to be anti-correlated with swarms periods with few events occurring while the plant is shutdown, as might be expected if we assume that events are purely induced by pore pressure increase.

The location of swarm activity in our catalog is much the same as was reported by Sewell et al. (2015a, Figure 5), with events occurring preferentially along the CFF, but with two other distinct clusters, one near RK23 and the other approximately 1 km to the north of RK23. The magnitude-frequency distribution of these events has a significantly lower b-value (0.77±0.03) (Figure 10) than the catalog as a whole (1.09±0.02). We interpret the relative abundance of large-magnitude events as an indication that swarm events are indeed occurring preferentially on the CFF, perhaps the only structure on which seismicity of M_L>3.0 (a rupture area of ∼0.1 km^2 **Stein and Wysession**) can occur within the field and which is optimally oriented for failure in the regional stress field.

5 Spatial *b*-value variations

Figures 11 and 12 reveal a complex pattern of b within the Rotokawa reservoir that defies simple explanation. Bachmann et al. (2012) modeled b-value for the case of the Basel enhanced geothermal injection well with

linearly increasing flow rate and linear pore-fluid pressure diffusion, showing that b is expected to decrease exponentially with distance from a given injection point. They found that this exponential b-value decay held for their catalog at distances greater than 200 m from the wellbore, but that b actually increased between the wellbore and 200 m, for reasons that weren't immediately clear. At Rotokawa, we observe a similarly complex pattern of b.

The higher b-value of the southeastern compartment as a whole, shown in Figure 5C, is also discernible in Figure 11 (map view). However, b is not uniform in space throughout any of the compartments. A profile of b-value for all compartments combined with distance from well RK23 or RK24 is shown in Figure 12C, but does not reveal any systematic behavior.

If we use the inferred IFF to divide the b-values into eastern and western compartments, on the basis that the pressure evolution on either side of the fault would be decoupled, the profiles take the shape of those in Figure 12A and B. In the western compartment (Figure 12B), b generally decays with distance from the well out to approximately 1 km, as predicted by the geomechanical modeling of (Bachmann et al., 2012), but increases from 1 km outwards. East of the IFF, b-value behavior is even more complicated, increasing from $b \approx 1.1$ near RK23, to $b > 1.5$ at a distance of 650 m before decaying at greater distances.

Similar to Bachmann et al. (2012), we observe an increase in b from the wellbore out to at least 150 m in all compartments. This may be an effect of near-well cooling, wherein the stabilization of the fracture network due to reservoir contraction counteracts the buildup in pore-pressure and suppresses failure on non-critically stressed fractures (Jeanne et al., 2015b). With distance from the well, thermal cooling will decay more quickly than pore-pressure perturbation. This may lead to a situation in which cooling effects dominate near the well, acting to suppress b-value, but give way to pore-pressure perturbations further afield, thereby increasing b-value via the processes described by Bachmann et al. (2012).

For all compartments, b-value also shows a depth dependence wherein b decreases from the surface to a minimum of $b \approx 0.9$ at 2.5 km (roughly the depth of injection) and then increases with depth until the base of seismicity at roughly 4 km. This appears counterintuitive, given the currently-accepted reasoning that b-value is inversely proportional to differential stress (σ_D), which generally increases with increasing overburden at depth (Schorlemmer et al., 2005). However, b-value has been shown to increase with depth in certain locations, especially in volcanic areas (e.g. Wiemer et al., 1998), perhaps owing to some combination of pervasive fracturing near intrusive bodies, high pore pressures, changing thermal gradients and an increase in host rock heterogeneity (Schorlemmer et al., 2005; Wiemer et al., 1998; Warren and Latham, 1970). All of these characteristics are certainly present at Rotokawa, which image logs and well cuttings have revealed to be highly-fractured and geologically heterogeneous reservoir (Massiot et al., 2015; McNamara et al., 2015). However, very little is known about what lies beneath New Zealand geothermal fields, why they exist where they do or how they are fed (Wilson and Rowland, 2016). Evidence from drilling at Ngatamariki has shown that intrusive bodies do exist at depths <3 km in the Taupo Volcanic Zone (Chambefort et al., 2016) and geochemical evidence suggests a similar intrusive body may sit below Rotokawa (Winick et al., 2009). However, the true nature of the heat source is far from certain (Wilson and Rowland, 2016).

Unfortunately, it is difficult to make the case that geologic heterogeneity and the degree of fracturing increase with depth below the base of the reservoir, as the reservoir itself is already both heterogeneous and highly-fractured (McNamara et al., 2015; Massiot et al., 2015). What's more, pore pressure perturbations originating at the injection wells decay with distance, making it yet more difficult to explain high b-values above or below the injection feedzones.

It is possible, that the depths presented for our catalog are systematically too deep, likely due to our lack of knowledge of the S-wave velocity structure in the field. Errors reported by bootstrap resampling of the input data used by *GrowClust* indicate average horizontal uncertainties of 200 m and average depth uncertainties of 278 m. However, we relocated the catalog using only P-picks, and also using $V_P V_S$ ratios of 1.86 and 2.0 (compared to $V_P V_S = 1.72$ presented here), all of which failed to change the depth dependence of b-value in the catalog. Once work is completed on a 3-D tomographic model of the Ngatamariki and Rotokawa

geothermal fields (by Steven Sewell), we may be better able to shed light on the depth uncertainties of seismicity at Rotokawa.

6 Conclusions

Over its two decades of development, the Rotokawa reservoir has been relatively well studied. The current understanding of the reservoir is based on research from a number of workers who have identified at least four compartments, which are likely bounded by a number of faults acting as barriers to inter-compartment flow (Sewell et al., 2015b; Addison et al., 2017; Wallis et al., 2013). Previous studies of microseismicity at Rotokawa have been used to constrain the location of one of these structures, the Central Field Fault, but due to its confinement to the injection field compartment, seismicity has been unable to reveal further structure within the reservoir (Sherburn et al., 2015; Sewell et al., 2015a).

Here we analyze a four-year catalog of seismicity from 2012–2015, corresponding to the four years immediately following the analysis of (Sherburn et al., 2015) and (Sewell et al., 2015a). While seismicity during these four years is still apparently confined to the injection field compartment, our catalog is better able to identify structures within this compartment, possibly revealing further compartmentalization in the injection field. The locations presented are able to further constrain the location and orientation of the Central Field Fault, and for the first time define the location of the Injection Field Fault, previously mapped only through vertical well cutting offsets and temperature gradients between wells. In addition, we have identified what may be a new structure, cutting across the dominant NE-SW structural grain. This structure may help explain the apparent pressure 'leak' between the injection field and central production compartment identified by tracer testing (Addison et al., 2017), where previously no pressure support was identified.

In addition, we have mapped the magnitude-frequency distribution (b-value) for the catalog. The pattern revealed is complex and fails to conform to a simplified model wherein b decays exponentially with distance from a pressure source (Bachmann et al., 2012). However, b does show a contrast between the compartments revealed from hypocentral locations. Specifically, b is higher to the east of the Injection Field Fault, suggesting that pressure may not be diffusing as readily in this section of the injection field, allowing non-critically stressed fractures to fail more often than in other compartments. It is possible that b-mapping at fields elsewhere could help to identify areas of the reservoir with large pressure gradients or changes in the degree of fracturing, which might exhibit as changes in the seismic b-value. In general, we believe these and other similar uses of earthquake magnitude information are under utilized as a tool for reservoir understanding and management.

7 Appendices

7.1 Location uncertainties

There are obvious differences between the hypocenters presented here and those presented by Sherburn et al. (2015); Sewell et al. (2015a). While it is possible, although unlikely, that these location differences represent a real migration of seismicity, there are at least two other potential causes for this, which we will discuss in detail here. The first is the location algorithm used to obtain the finalized, double-difference locations and the other is the significant uncertainty in the velocity structure at the geothermal fields.

In order to illustrate the potential contribution of the different location algorithms to the variations in earthquake hypocenters, we relocated a subset of an earlier GNS Science catalog containing only manual phase picks using two algorithms: *GrowClust* (this study) (Trugman and Shearer, 2017) and *HypoDD* Sherburn et al. (2015); Sewell et al. (2015a); Waldhauser and Ellsworth (2000). The locations for each are shown in Figures 13 (*HypoDD*) and 14 (*GrowClust*). The workflow and velocity model used to obtain the GNS Science locations is unknown. For the *GrowClust* locations, we located the catalog from scratch with *NonLinLoc*

(Lomax et al., 2014), using the velocity model from Sewell et al. (2017), before relocating the catalog with GrowClust.

As stated above, the locations provided by GNS Science broadly agree with the depths of the major feedzones for the main injection wells (<2000 m bsl), particularly RK24, although a number of events occur at shallower depths (Figure 13). Our *GrowClust* locations cluster more tightly, especially in cross-section. Those events occurring nearest RK24 are in better agreement with the depth of the feedzones than the *HypoDD* locations. In map view, these events also define a structure striking NE-SW, consistent with the regional trend and perhaps associated with the Injection Field Fault, which had been inferred from stratigraphic offsets between the three main injection wells RK20, RK23 and RK24, which were all drilled from the same wellpad (Sewell et al., 2015b).

While the *GrowClust* locations are more consistent with known structures and feedzone depths in the deep reservoir, it is nevertheless difficult to state with certainty that they are the 'correct' locations. Figures 13 and 14 simply serve to show that, using the same data, variations in velocity model and especially location algorithm can produce hypocenters that may yield different interpretations.

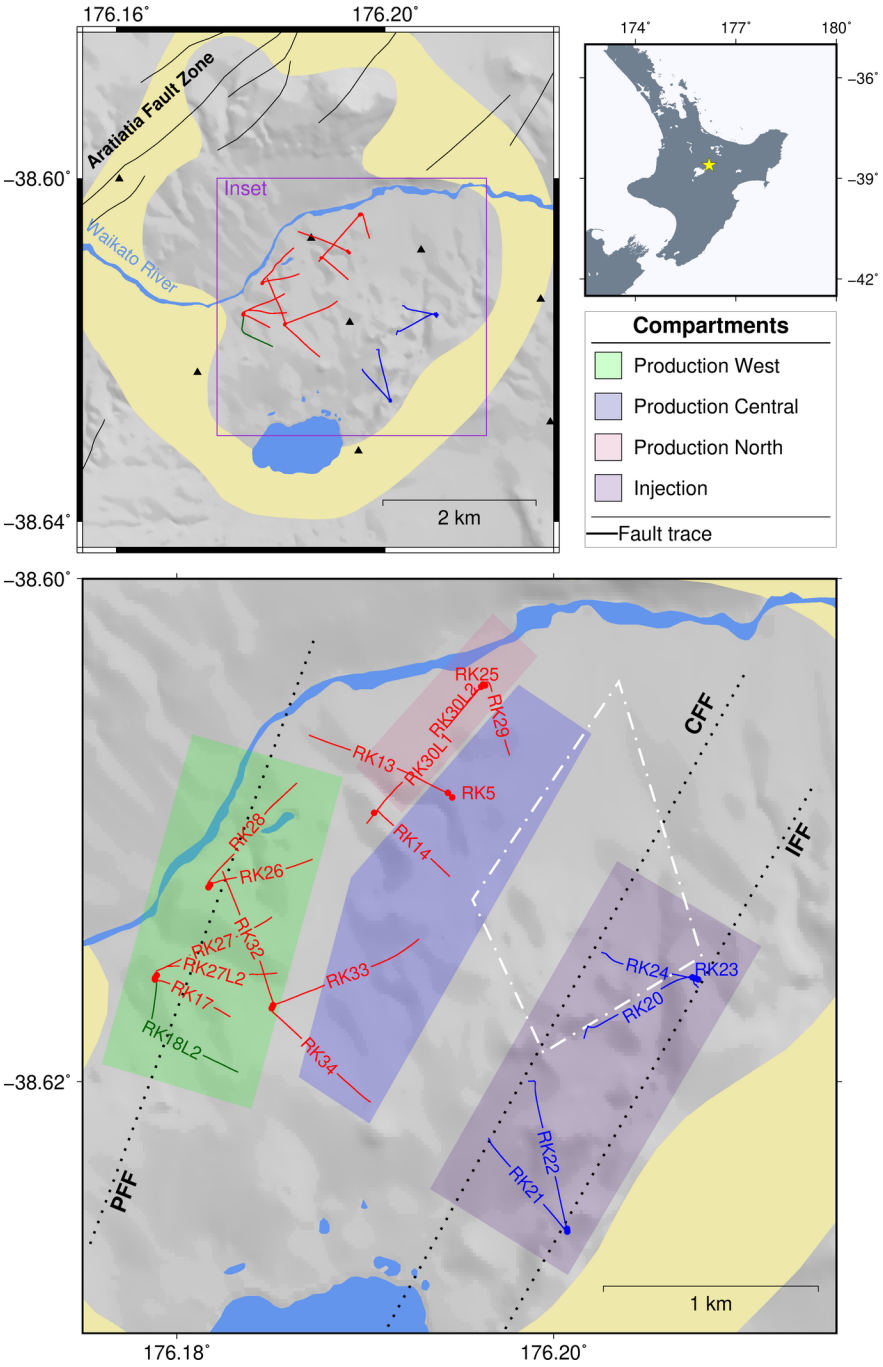

Figure 1: Overview of the Rotokawa geothermal field. The top right panel shows the location of the field on the North Island of New Zealand (yellow star). The top left panel shows the resistivity boundary of the field in yellow and injection and production wells in blue and red, respectively. Solid black lines are active faults. The lower panel shows a closeup of the field, with the well names labeled and the three known faults (PFF, CFF, IFF) shown as black dotted lines. The white dot-dashed line shows the extent of significant seismicity from 2008-2012, as reported by Sherburn et al. (2015). There are four known compartments in the Rotokawa reservoir shown as colored polygons. Each is semi-isolated from the others by either a permeability contrast or impermeable barrier (i.e. a fault). The production field comprises three compartments, the west, central and north (green, blue and red, respectively). The injection field is shaded in purple and is a separate compartment.

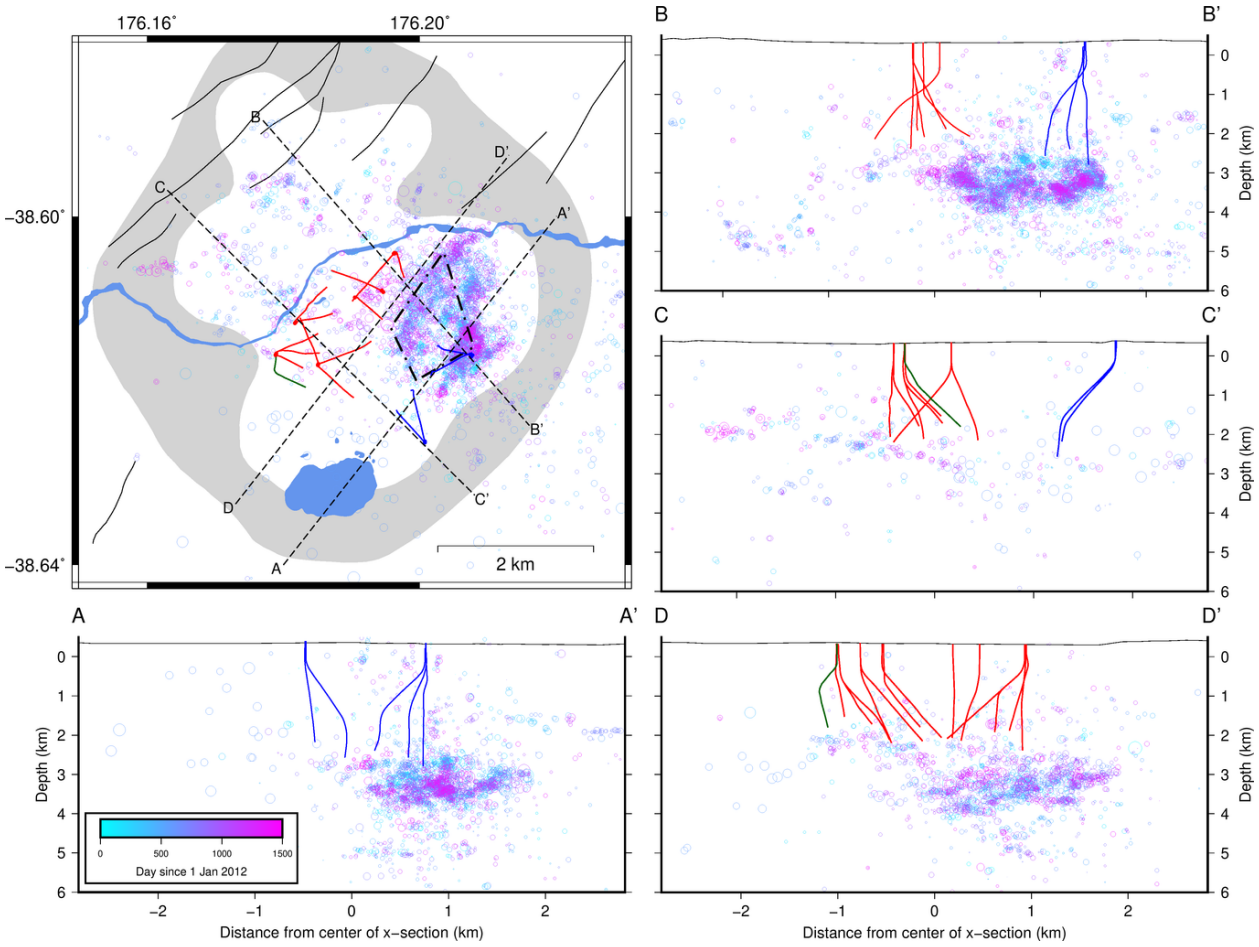

Figure 2: Seismicity at Rotokawa for the years 2012-2015 colored by date of occurrence. Blue events occurred earlier in the dataset and pink events occurred later. Four cross sections are plotted to show the depth distribution of seismicity and their surface projections are shown in map view. The dot-dashed diamond indicates the area of dense seismicity identified by Sherburn et al., 2015; Sewell et al., 2015a for the 2008-2012 catalog.

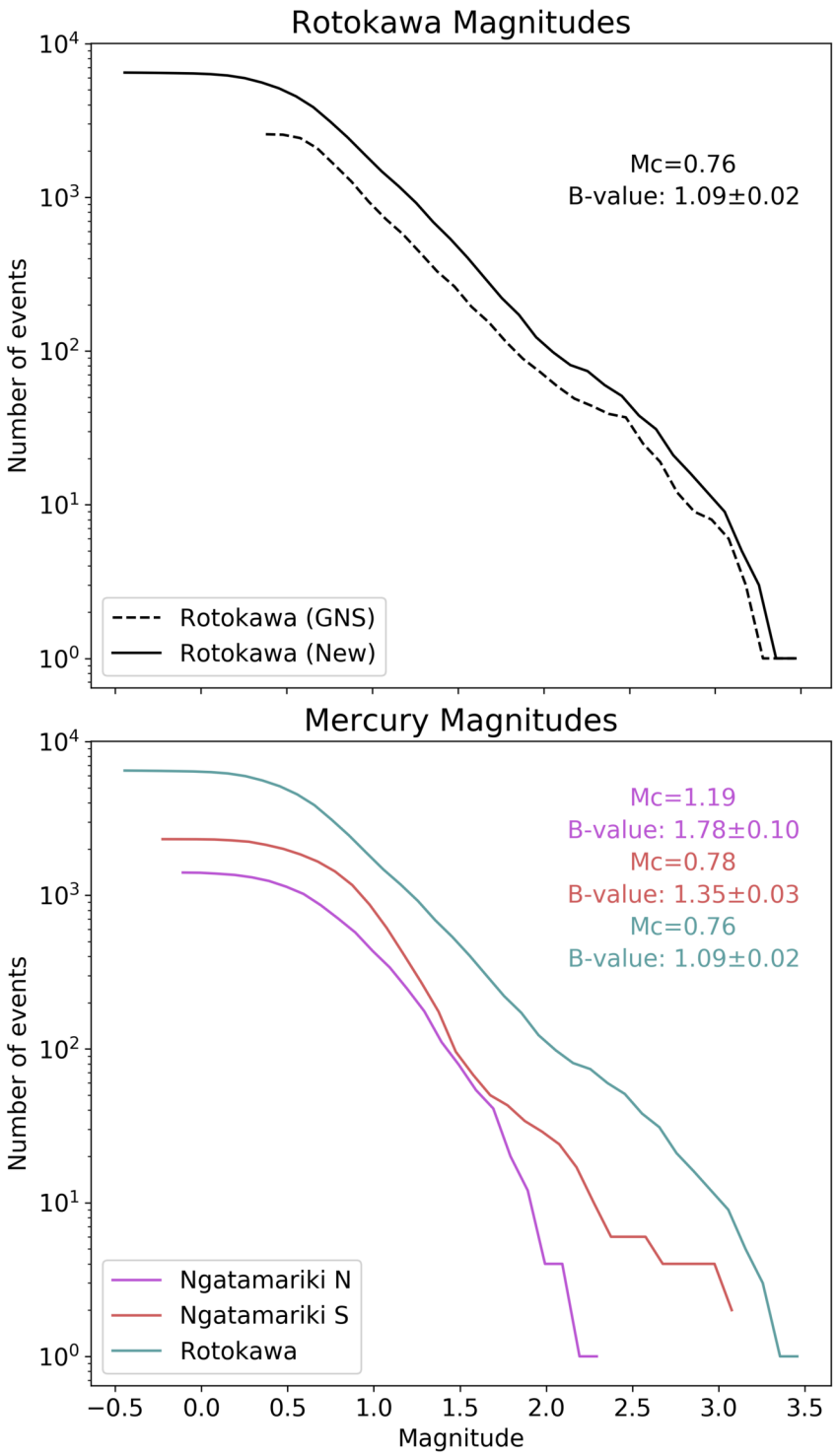

Figure 3: Top panel: Frequency-magnitude distributions for the GNS (dotted) and matched-filter-detected (solid) catalogs at Rotokawa from 2012-2015. The calculated magnitude of completeness and b-value are noted in the top right for the matched-filter catalog. Bottom panel: Frequency-magnitude distributions compared for Northern Ngatamariki, Southern Ngatamariki and Rotokawa. The Mc and b-value for each catalog is noted in the top right, consistent with the catalog order in the legend.

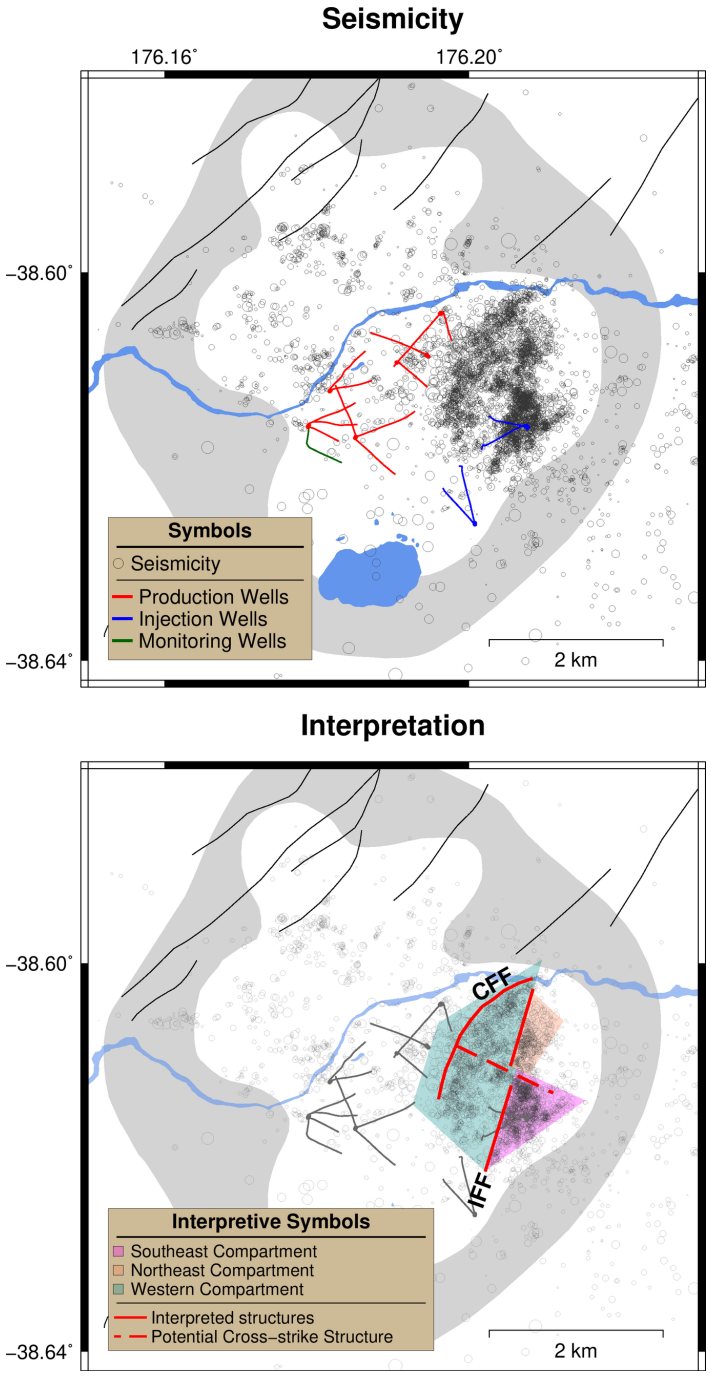

Figure 4: Seismicity at Rotokawa from 2012-2015, relocated with GrowClust. The top panel shows seismicity as black circles, scaled to each earthquake's magnitude (as in Figure 2). The bottom panel shows our interpretation of reservoir structure from the location of seismicity (red lines). These structures may define reservoir compartments (colored regions). The location and orientation of the Central Field Fault and Injection Field Fault (solid red) are well constrained from seismicity. In addition, the dotted red line indicates the location of a possible cross-strike structure north of the injection field, which may contribute to further injection-field compartmentalization.

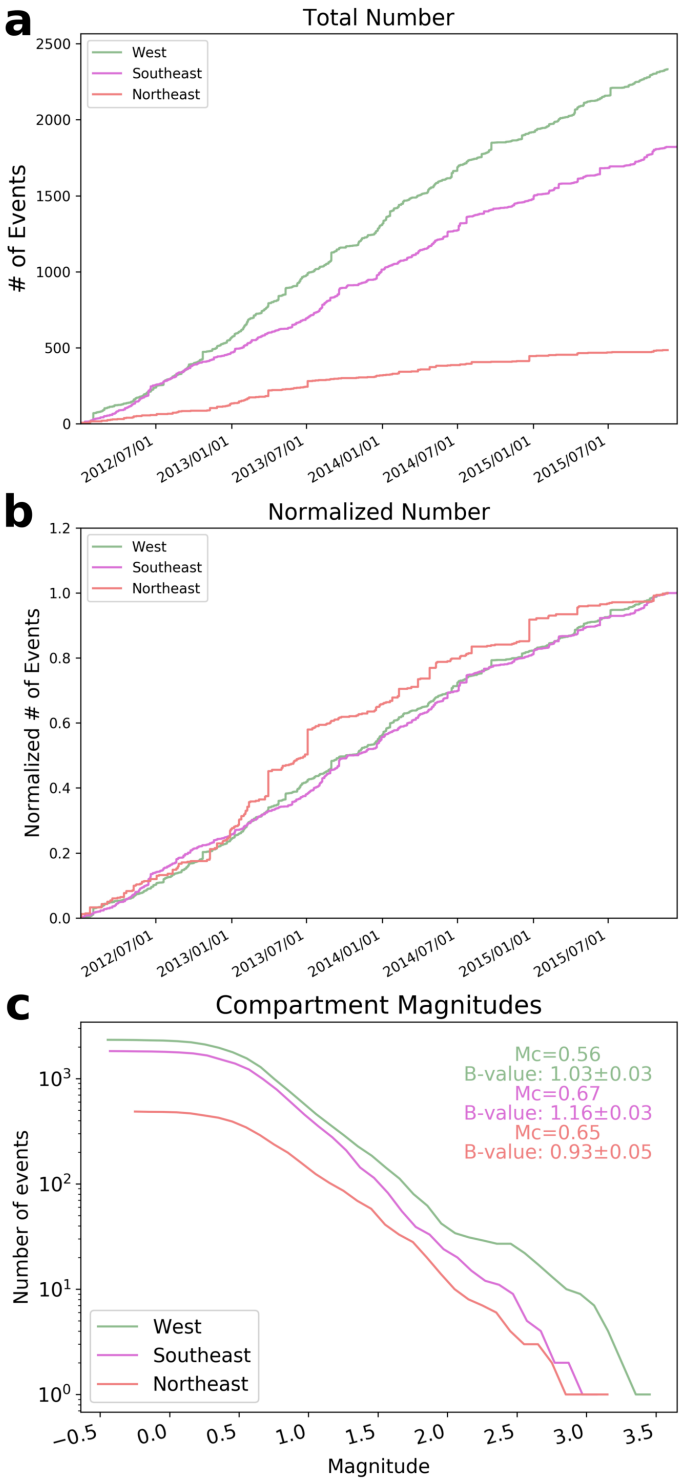

Figure 5: a) Total and b) normalized cumulative number of earthquakes in each of the three compartments defined in Figure 4 . c) Frequency-magnitude distributions for each of the compartments.

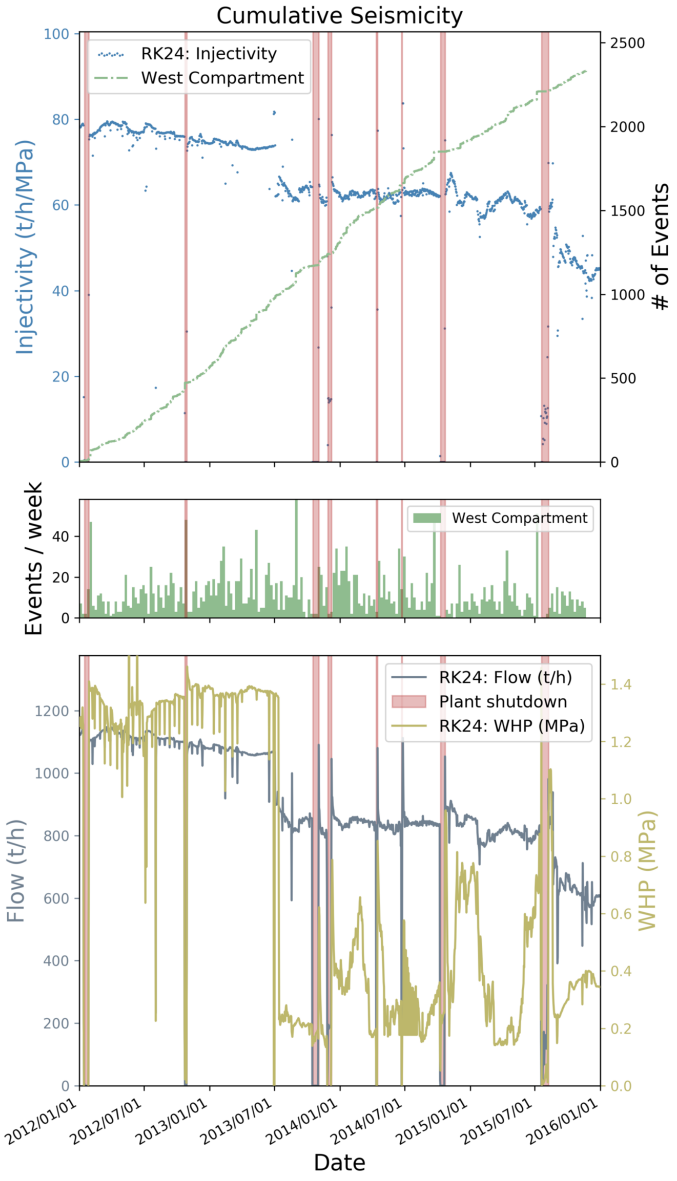

Figure 6: Seismicity in the western compartment defined above compared to well parameters for well RK24. The top panel shows the cumulative number of events (green dot-dashed) with injectivity at RK24 (blue). The middle panel shows the weekly rate of seismicity in the western compartment. The bottom panel shows both flow rate (dark gray) and wellhead pressure (yellow). Red shaded regions in all panels indicate the periods during which the power plants were shut down for maintenance, which have been recognized previously as periods of potentially heightened seismicity.

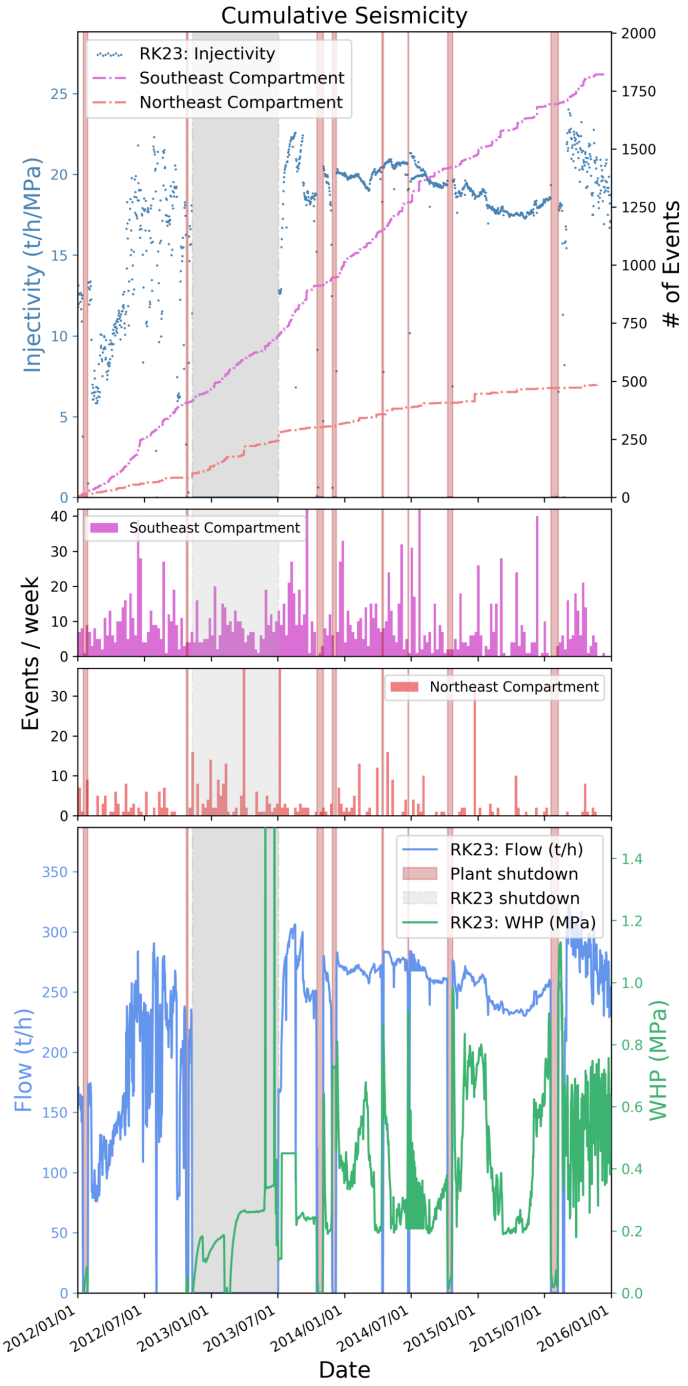

Figure 7: Seismicity in the eastern compartments defined above compared to well parameters for well RK23. The top panel shows the cumulative number of events (magenta and coral colored lines) with injectivity at RK23 (blue). The middle two panels show the weekly rate of seismicity in the southeastern and northeastern compartments, respectively. The bottom panel shows both flow rate (blue) and wellhead pressure (green). Red shaded regions in all panels indicate the periods during which the power plants were shut down for maintenance, which have been recognized previously as periods of potentially heightened seismicity. The period of time during which RK23 was shut is shaded in gray.

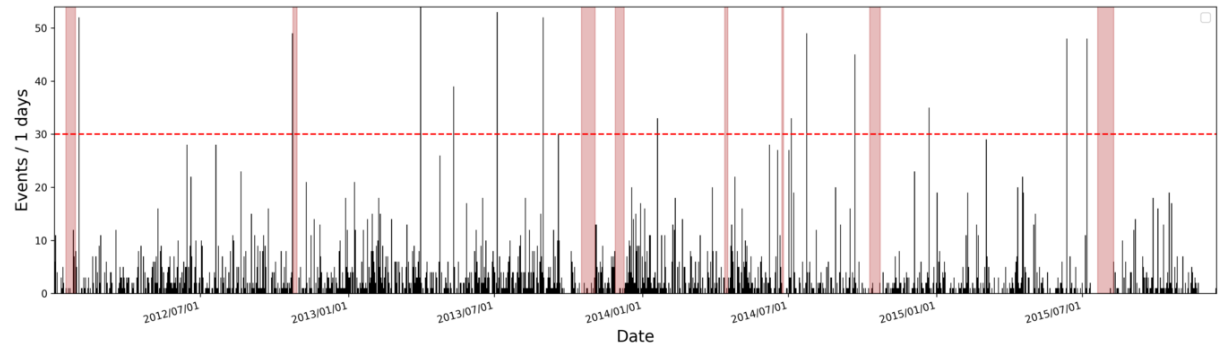

Figure 8: Daily rate of seismicity at Rotokawa. The red dotted line indicates the threshold used to define the days corresponding to 'swarm' events.

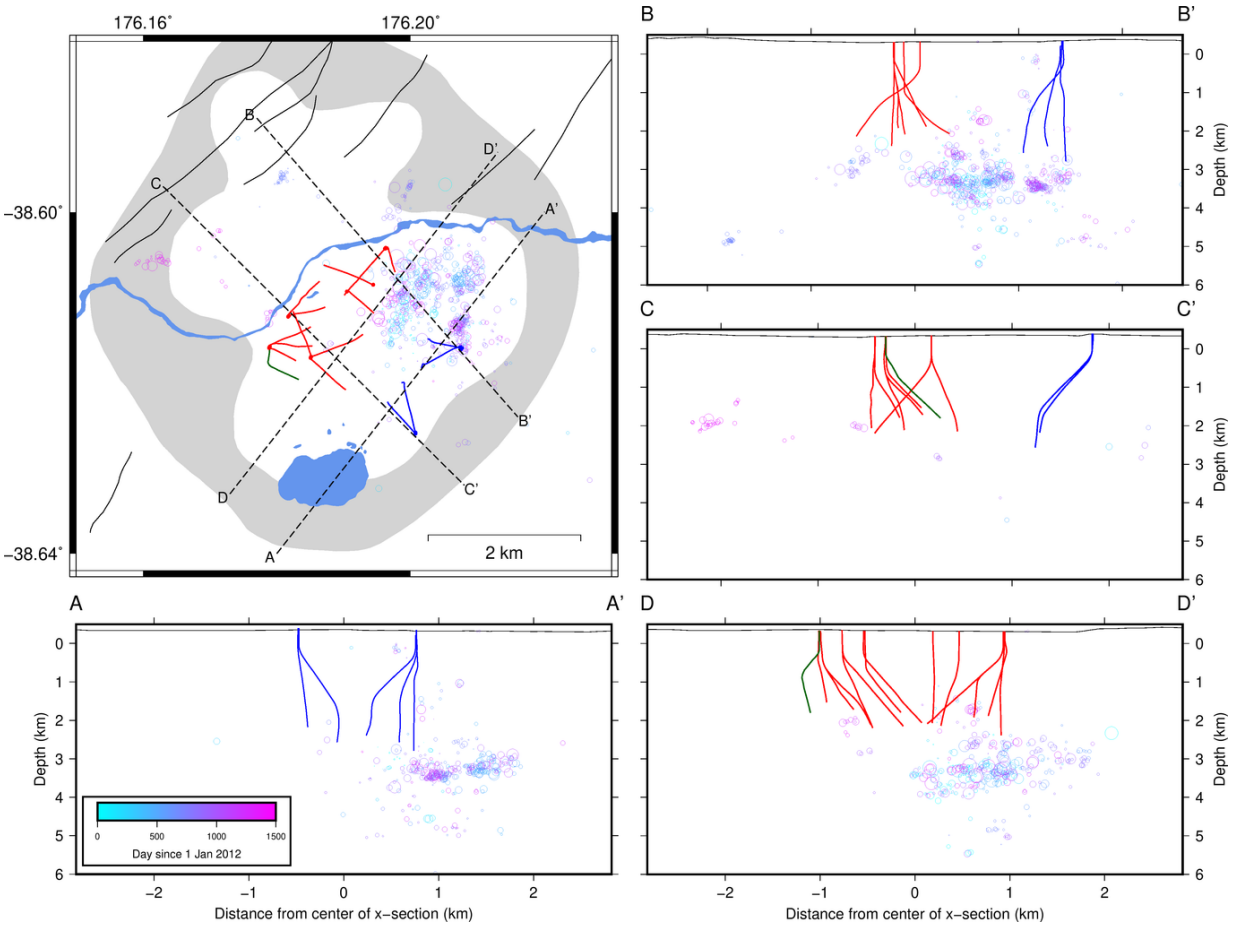

Figure 9: 'Swarm-like' events at Rotokawa. Swarms were defined as days on which more than 30 events occurred.

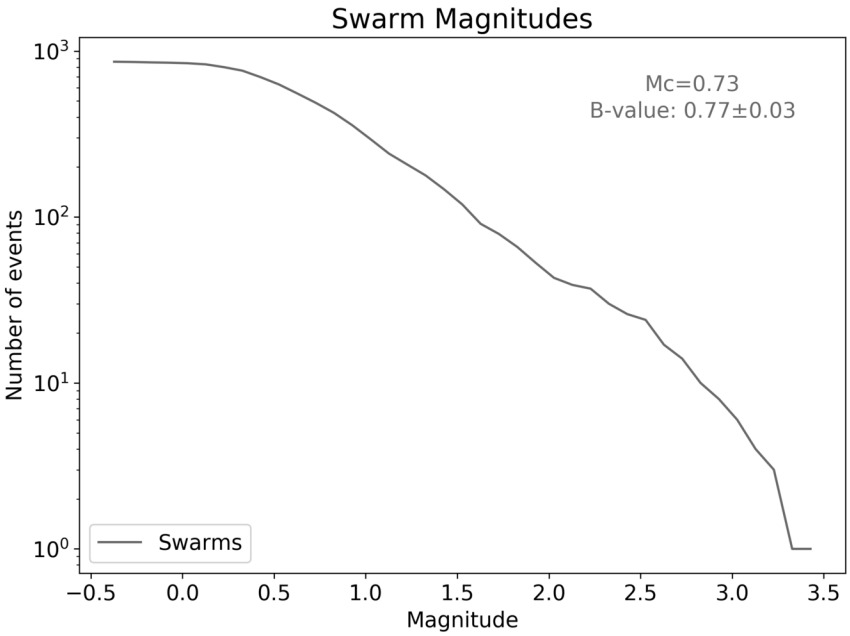

Figure 10: Frequency-magnitude distribution of events occurring on days of heightened seismicity (i.e. 'swarms').

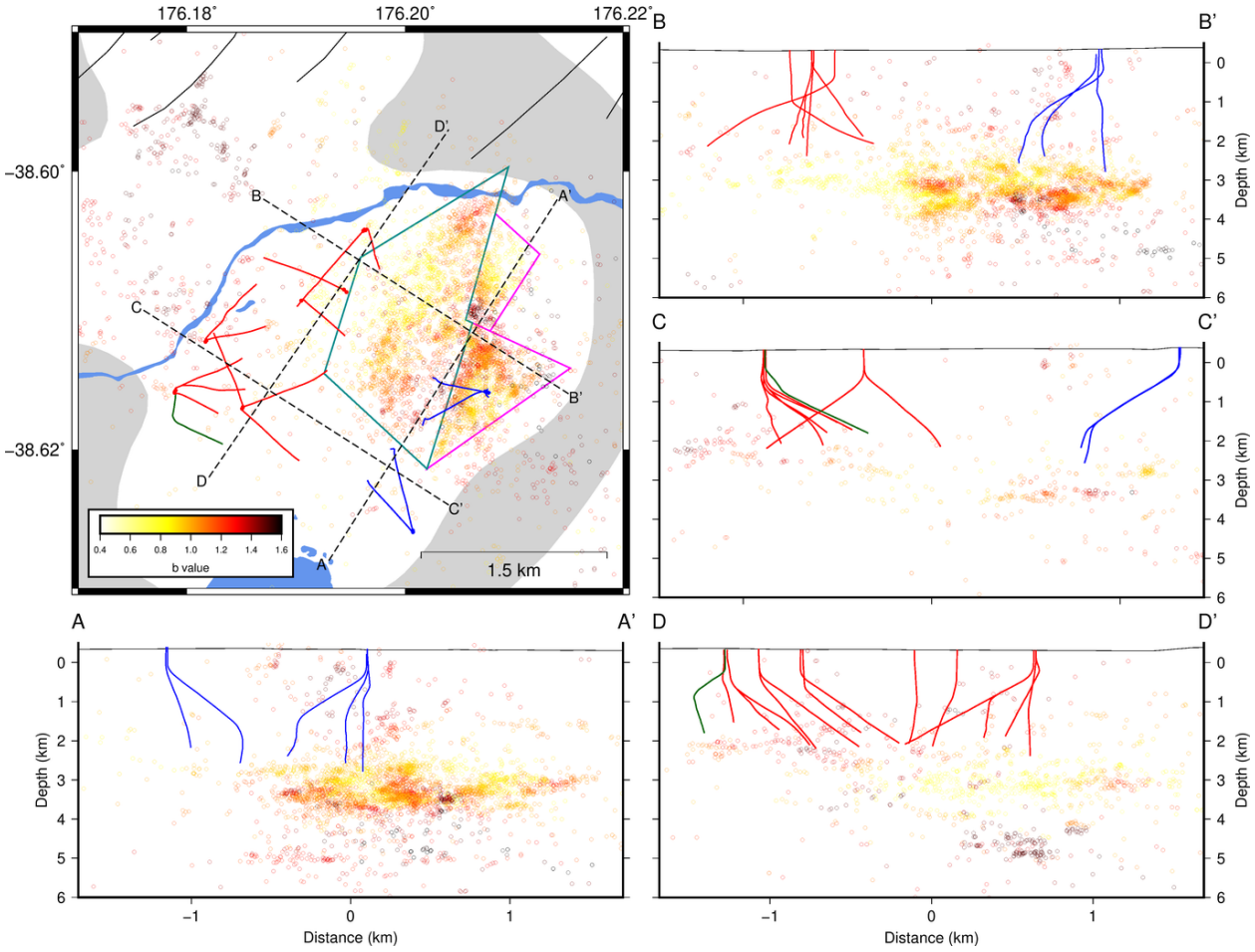

Figure 11: Spatial variation in b-value at Rotokawa. Events are colored by b-value, calculated using the nearest 300 events, provided there are at least 100 events greater than the Mc. The western compartment defined above is outlined in green and the two eastern compartments are outlined in pink.

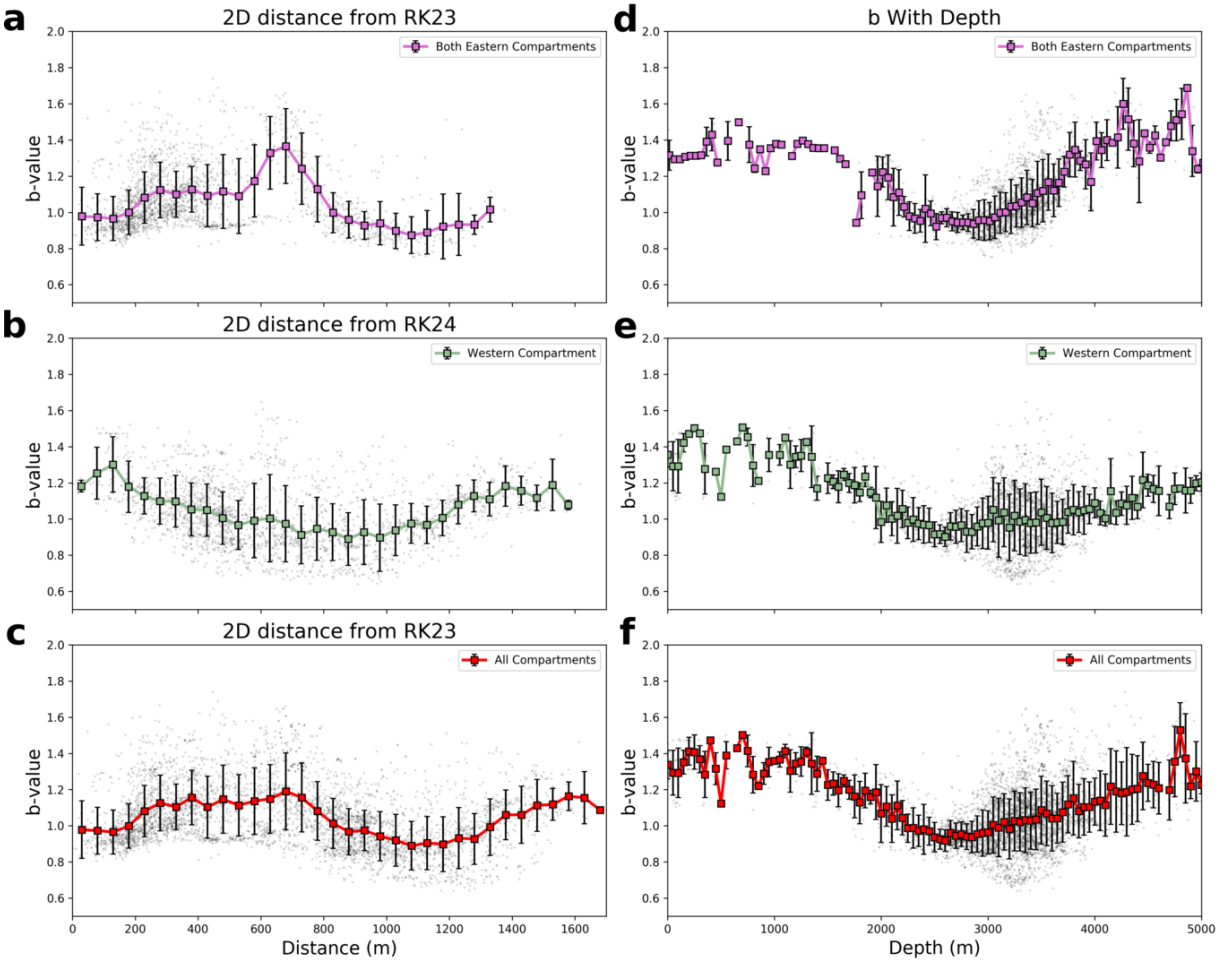

Figure 12: b values with 2-dimensional radius from the bottom of injection well RK23 (panels a and c) or RK24 (panel b). Panel a) shows the distance from RK23 to all events in both eastern compartments, combined. Panel b) shows the distance from well RK24 to all events in the western compartment. Panel c) shows the distance from RK23 to all events in the catalog. Markers show the average and bars show the standard deviation in each distance bin. Panels d, e and f show the b-value distribution with depth for the catalogs in panels a, b and c.

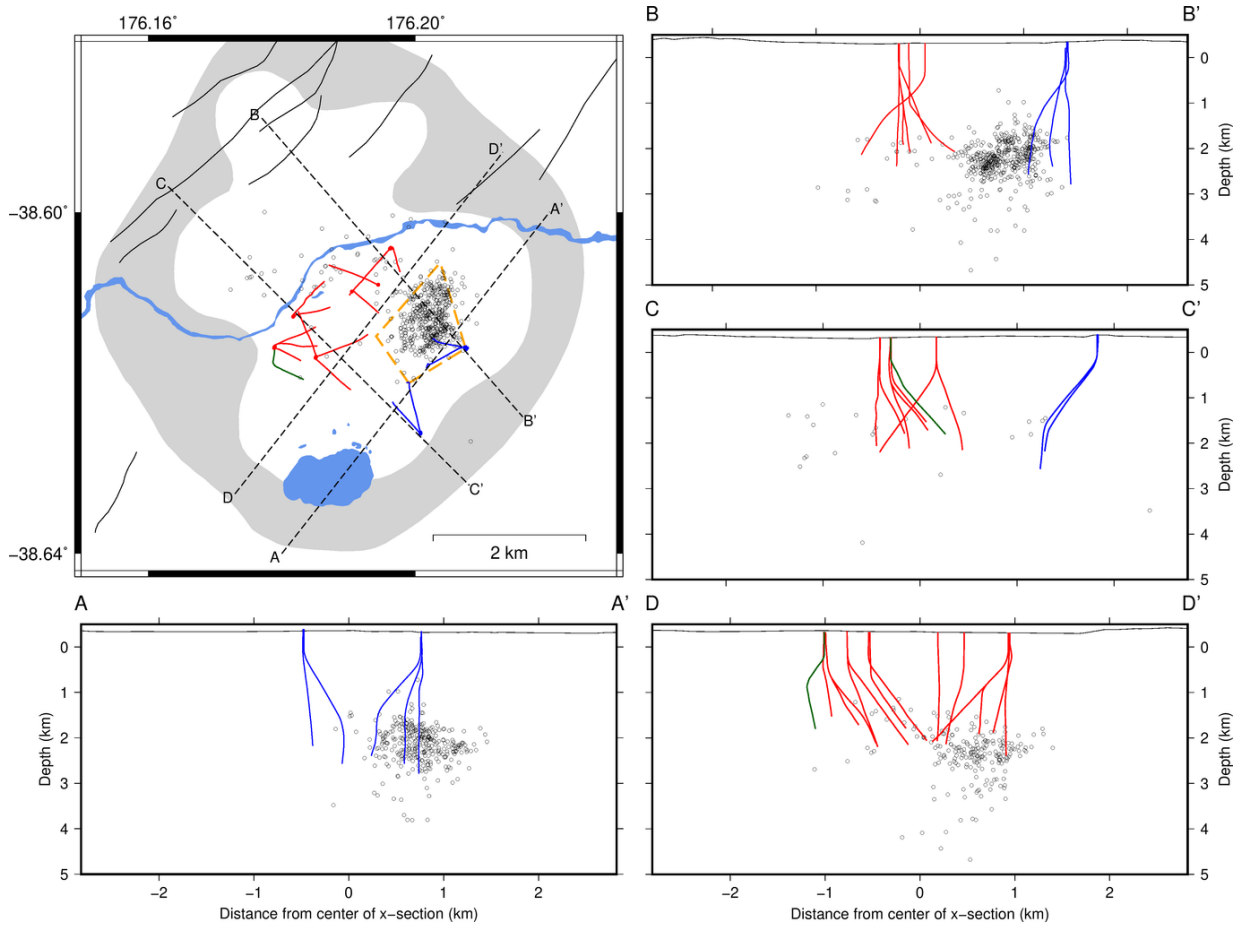

Figure 13: GNS Science manual phase picks for 2012-2013, relocated with *HypoDD*. The orange, dotted diamond is the area defined by Sherburn et al. (2015) as the active seismic zone as of the end of 2012.

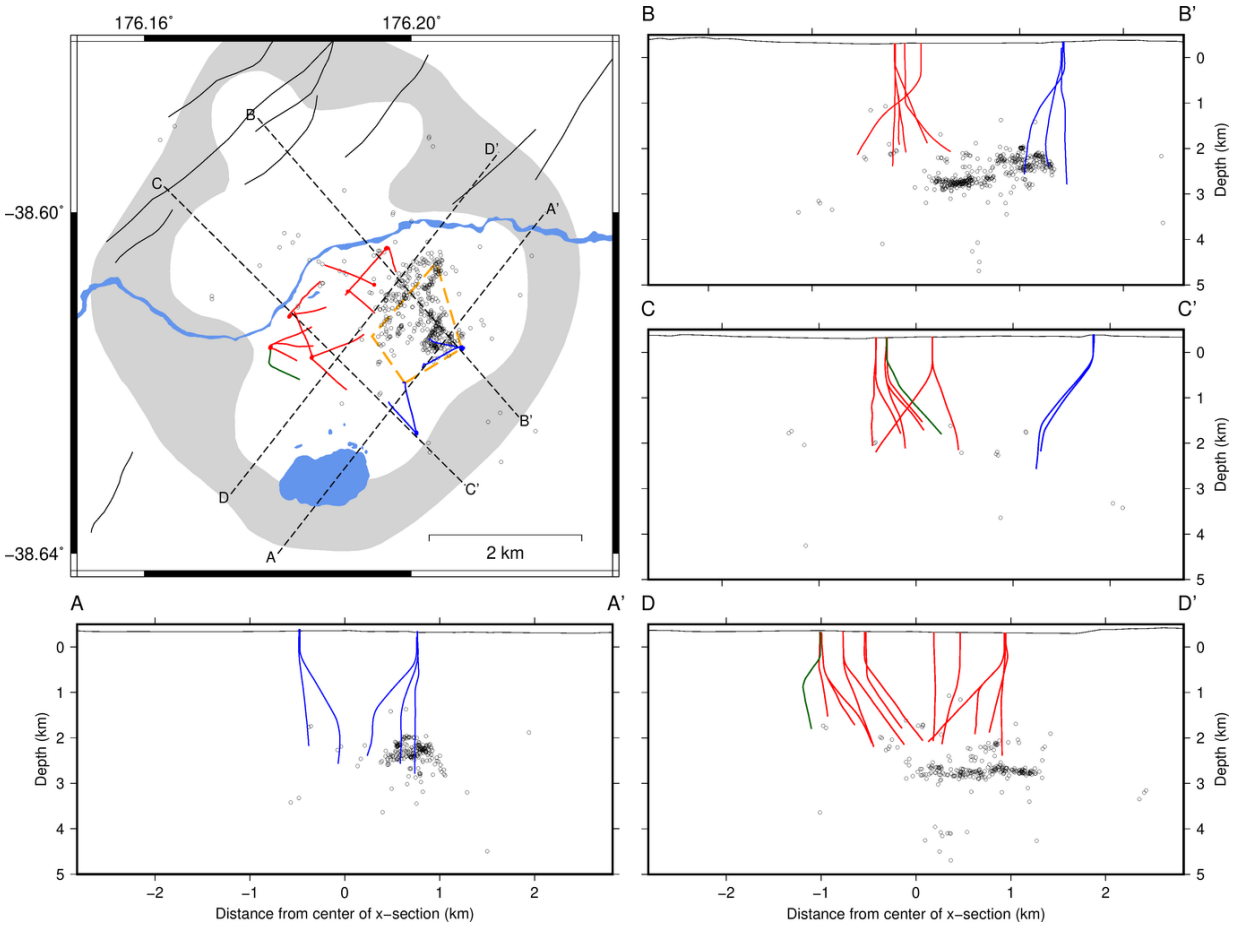

Figure 14: GNS Science manual phase picks for 2012-2013, relocated with *GrowClust*. As above, the orange diamond identifies the area of active seismicity as of the end of 2012, defined by the locations in Figure 13 . Here, the hypocenters are more tightly clustered, but occupy a larger overall footprint than the GNS Science locations.

References

S. Addison, L. Sirad-Azwar, J. Clearwater, D. Hernandez, B. Mountain, A. Blair, and P. Siratovich. Improving the conceptual understanding through a recent injection of 200 GBq of iodine-125 at the Rotokawa geothermal field, New Zealand. In *42nd Workshop on Geothermal Reservoir Engineering*, 2017.

SJ Addison, JA Winick, BW Mountain, and FL Siega. Rotokawa reservoir tracer test history. In *Proc. NZ Geothermal Workshop*, 2015.

Keiiti Aki. Maximum likelihood estimate of b in the formula log N= a-bM and its confidence limits. *Bull. Earthq. Res. Inst., Tokyo Univ.*, 43:237–239, 1965.

C. E. Bachmann, S. Wiemer, B. P. Goertz-Allmann, and J. Woessner. Influence of pore-pressure on the event-size distribution of induced earthquakes. *Geophysical Research Letters*, 39(9):n/a–n/a, May 2012. doi: 10.1029/2012gl051480. URL https://doi.org/10.1029%2F2012gl051480.

Isabelle Chambefort, Etienne Buscarlet, Irene C. Wallis, Steven Sewell, and Maxwell Wilmarth. Ngatamariki Geothermal Field New Zealand: Geology, geophysics, chemistry and conceptual model. *Geothermics*, 59:266–280, Jan 2016. doi: 10.1016/j.geothermics.2015.07.011. URL https://doi.org/10.1016%2Fj.geothermics.2015.07.011.

Jonathon Clearwater, Lutfhie Azwar, Mike Barnes, Irene Wallis, and Robert Holt. Changes in injection well capacity during testing and plant start-up at Ngatamariki. In *World Geothermal Congress*, 2015.

B Cole and H Legmann. The Rotokawa Geothermal Project-A High Pressure, Sustainable and Environmentally Benign Power Plant. *TRANSACTIONS-GEOTHERMAL RESOURCES COUNCIL*, pages 509–514, 1998.

Carsten Dinske and Serge A. Shapiro. Seismotectonic state of reservoirs inferred from magnitude distributions of fluid-induced seismicity. *Journal of Seismology*, 17(1):13–25, Mar 2012. doi: 10.1007/s10950-012-9292-9. URL https://doi.org/10.1007%2Fs10950-012-9292-9.

Julio Garcia, Craig Hartline, Mark Walters, Melinda Wright, Jonny Rutqvist, Patrick F. Dobson, and Pierre Jeanne. The Northwest Geysers EGS Demonstration Project California. *Geothermics*, 63:97–119, Sep 2016. doi: 10.1016/j.geothermics.2015.08.003. URL https://doi.org/10.1016%2Fj.geothermics.2015.08.003.

Beno Gutenberg and Charles Francis Richter. Earthquake magnitude, intensity, energy, and acceleration. *Bulletin of the Seismological Society of America*, 32(3):163–191, 1942.

Chet Hopp, Steven Sewell, Stefan Mroczek, Martha Savage, and John Townend. Seismic Response to Injection Well Stimulation in a High-Temperature, High-Permeability Reservoir. *Geochemistry, Geophysics, Geosystems*, 2019.

Pierre Jeanne, Jonny Rutqvist, Patrick F. Dobson, Julio Garcia, Mark Walters, Craig Hartline, and Andrea Borgia. Geomechanical simulation of the stress tensor rotation caused by injection of cold water in a deep geothermal reservoir. *Journal of Geophysical Research: Solid Earth*, 120(12):8422–8438, Dec 2015a. doi: 10.1002/2015jb012414. URL https://doi.org/10.1002%2F2015jb012414.

Pierre Jeanne, Jonny Rutqvist, Patrick F Dobson, Julio Garcia, Mark Walters, Craig Hartline, and Andrea Borgia. Geomechanical simulation of the stress tensor rotation caused by injection of cold water in a deep geothermal reservoir. *Journal of Geophysical Research: Solid Earth*, 120(12):8422–8438, 2015b.

Katie M Keranen and Matthew Weingarten. Induced seismicity. *Annual Review of Earth and Planetary Sciences*, 46:149–174, 2018.

Hilel Legmann and Phillip Sullivan. The 30 MW Rotokawa I geothermal project five years of operation. In *International geothermal conference*, pages 26–31, Reykjavik, 2003.

Anthony Lomax, Alberto Michelini, and Andrew Curtis. Earthquake location: Direct, global-search methods. In *Encyclopedia of Complexity and Systems Science*, pages 1–33. Springer New York, 2014. doi: 10.1007/978-3-642-27737-5_150-2. URL https://doi.org/10.1007%2F978-3-642-27737-5_150-2.

Cécile Massiot, John Townend, David D McNamara, and Andrew Nicol. Fracture width and spacing distributions from borehole televiewer logs and cores in the Rotokawa Geothermal Field, New Zealand. In *World Geothermal Congress 2015*. International Geothermal Association, 2015.

David D McNamara, Cécile Massiot, Brandon Lewis, and Irene C Wallis. Heterogeneity of structure and stress in the Rotokawa Geothermal Field, New Zealand. *Journal of Geophysical Research: Solid Earth*, 120(2):1243–1262, 2015.

David Daniel McNamara, Steven Sewell, Etienne Buscarlet, and Irene C. Wallis. A review of the Rotokawa Geothermal Field New Zealand. *Geothermics*, 59:281–293, Jan 2016. doi: 10.1016/j.geothermics.2015.07.007. URL https://doi.org/10.1016%2Fj.geothermics.2015.07.007.

National Academy of Sciences. *Induced Seismicity Potential in Energy Technologies*. National Academies Press, aug 2013. doi: 10.17226/13355. URL https://doi.org/10.17226%2F13355.

J. Quinao, L. Sirad-Azwar, J. Clearwater, V. Hoepfinger, M. Le Brun, and C. Bardsley. Analyses and modeling of reservoir pressure changes to interpret the Rotokawa geothermal field response to Nga Awa Purua power station operation. In *38th Workshop on Geothermal Reservoir Engineering*, 2013.

M. Schoenball, C. Baujard, T. Kohl, and L. Dorbath. The role of triggering by static stress transfer during geothermal reservoir stimulation. *Journal of Geophysical Research: Solid Earth*, 117(B9), Sep 2012. doi: 10.1029/2012jb009304. URL https://doi.org/10.1029%2F2012jb009304.

Danijel Schorlemmer, Stefan Wiemer, and Max Wyss. Variations in earthquake-size distribution across different stress regimes. *Nature*, 437(7058):539–542, Sep 2005. doi: 10.1038/nature04094. URL https://doi.org/10.1038%2Fnature04094.

P. Segall. Earthquakes triggered by fluid extraction. *Geology*, 17(10):942, 1989. doi: 10.1130/0091-7613(1989)017<0942:etbfe>2.3.co;2. URL https://doi.org/10.1130%2F0091-7613%281989%29017%3C0942%3Aetbfe%3E2.3.co%3B2.

S. Sewell, M. Savage, J. Townend, S. Bannister, and L. Hutchings. Preliminary investigation of seismic velocity variation at the Rotokawa and Ngatamariki geothermal field. In *Proceedings 39th New Zealand Geothermal Workshop*, 2017.

S. M. Sewell, W. Cumming, C. J. Bardsley, J. Winick, I. C. Wallis, S. Sherburn, S. Bourguignon, and S. Bannister. Interpretation of Microseismicity at the Rotokawa Geothermal Field, 2008 to 2012. In *World Geothermal Congress*, 2015a.

S.M. Sewell, S.J. Addison, L. Azwar, and M.L. Barnes. Rotokawa Conceptual Model Update 5 years After Commissioning of the 138 MWe NAP Plant. In *Proceedings 37th New Zealand Geothermal Workshop*, volume 18, 2015b.

Serge A. Shapiro, Oliver S. Krüger, Carsten Dinske, and Cornelius Langenbruch. Magnitudes of induced earthquakes and geometric scales of fluid-stimulated rock volumes. *GEOPHYSICS*, 76(6):WC55–WC63, Nov 2011. doi: 10.1190/geo2010-0349.1. URL https://doi.org/10.1190%2Fgeo2010-0349.1.

S. Sherburn, S.M. Sewell, S. Bourguignon, W. Cumming, S. Bannister, C. Bardsley, J. Winick, J. Quinao, and I.C. Wallis. Microseismicity at Rotokawa geothermal field New Zealand, 2008–2012. *Geothermics*, 54:23–34, Mar 2015. doi: 10.1016/j.geothermics.2014.11.001. URL https://doi.org/10.1016%2Fj.geothermics.2014.11.001.

Yaolin Shi and Bruce A Bolt. The standard error of the magnitude-frequency b value. *Bulletin of the Seismological Society of America*, 72(5):1677–1687, 1982.

Ross S Stein. The role of stress transfer in earthquake occurrence. *Nature*, 402(6762):605, 1999.

George Stephens and Bo Voight. Hydraulic fracturing theory for conditions of thermal stress. In *International Journal of Rock Mechanics and Mining Sciences & Geomechanics Abstracts*, volume 19, pages 279–284. Elsevier, 1982.

Daniel T. Trugman and Peter M. Shearer. GrowClust: A Hierarchical Clustering Algorithm for Relative Earthquake Relocation with Application to the Spanish Springs and Sheldon, Nevada, Earthquake Sequences. *Seismological Research Letters*, 88(2A):379–391, Feb 2017. doi: 10.1785/0220160188. URL https://doi.org/10.1785%2F0220160188.

F. Waldhauser and W. Ellsworth. A Double-Difference Earthquake Location Algorithm: Method and Application to the Northern Hayward Fault California. *Bulletin of the Seismological Society of America*, 90 (6):1353–1368, Dec 2000. doi: 10.1785/0120000006. URL https://doi.org/10.1785%2F0120000006.

I. Wallis, C. Bardsley, T. Powell, J. Rowland, and J. O'Brien. A structural model for the Rotokawa Geothermal Field, New Zealand. In *Proceedings 35th New Zealand Geothermal Workshop*, 2013.

Nicholas W. Warren and Gary V. Latham. An experimental study of thermally induced microfracturing and its relation to volcanic seismicity. *Journal of Geophysical Research*, 75(23):4455–4464, Aug 1970. doi: 10.1029/jb075i023p04455. URL https://doi.org/10.1029%2Fjb075i023p04455.

S. Wiemer and M. Wyss. Minimum Magnitude of Completeness in Earthquake Catalogs: Examples from Alaska the Western United States, and Japan. *Bulletin of the Seismological Society of America*, 90(4): 859–869, Aug 2000. doi: 10.1785/0119990114. URL https://doi.org/10.1785%2F0119990114.

Stefan Wiemer and Stephen R. McNutt. Variations in the frequency-magnitude distribution with depth in two volcanic areas: Mount St. Helens Washington, and Mt. Spurr, Alaska. *Geophysical Research Letters*, 24(2):189–192, Jan 1997. doi: 10.1029/96gl03779. URL https://doi.org/10.1029%2F96gl03779.

Stefan Wiemer, Stephen R. McNutt, and Max Wyss. Temporal and three-dimensional spatial analyses of the frequency-magnitude distribution near Long Valley Caldera California. *Geophysical Journal International*, 134(2):409–421, Aug 1998. doi: 10.1046/j.1365-246x.1998.00561.x. URL https://doi.org/10.1046%2Fj.1365-246x.1998.00561.x.

Colin J.N. Wilson and Julie V. Rowland. The volcanic magmatic and tectonic setting of the Taupo Volcanic Zone, New Zealand, reviewed from a geothermal perspective. *Geothermics*, 59:168–187, Jan 2016. doi: 10.1016/j.geothermics.2015.06.013. URL https://doi.org/10.1016%2Fj.geothermics.2015.06.013.

J. Winick, T. Powell, and E. Mroczek. The natural-state geochemistry of the Rotokawa reservoir. In *Proceedings 31st New Zealand Geothermal Workshop*, 2009.